In Situ X-ray Diffraction Study of the Formation, Growth, and Phase Transition of Colloidal $Cu_{2-x}S$ Nanocrystals

Peter Nørby, Simon Johnsen, and Bo B. Iversen*

Center for Materials Crystallography, Department of Chemistry and iNANO, Aarhus University, Langelandsgade 140, DK-8000 Aarhus C, Denmark

ABSTRACT The formation, growth, and phase transition of colloidal monodisperse spherical copper sulfide nanocrystals synthesized in dodecanethiol have been followed by *in situ* synchrotron powder X-ray diffraction (PXRD). The formation of nanocrystals involves a thermal decomposition of the crystalline precursor [$CuSC_{12}H_{25}$], which upon heating forms an isotropic liquid that subsequently turns into colloidal β-chalcocite phase Cu_2S nanocrystals. The redox reaction step in the precursor solution has been studied by proton NMR. Upon heating, high digenite phase nanocrystals are formed through a solid-state rearrangement phase transition of the β-chalcocite phase nanocrystals at temperatures above 260 °C. TEM and PXRD reveal that the nanocrystal size is independent of synthesis temperature and stabilizes after the phase transition has completed. Spherical monodisperse nanocrystals are obtained in all experiments, with the nanocrystals in the β-chalcocite phase (7 nm) being smaller than those in high digenite phase (11 nm).

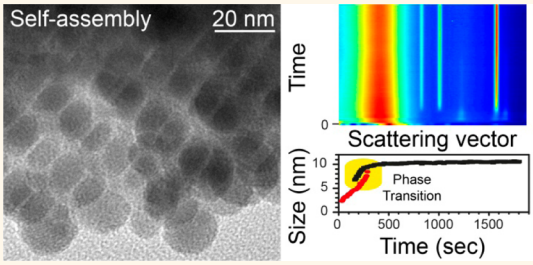

KEYWORDS: colloidal nanocrystals · *in situ* X-ray diffraction · $Cu_{2-x}S$ · phase transition · crystal growth

Colloidal metal chalcogenide semiconductor nanocrystals, for which physical and chemical properties can be modified by minute changes in morphology, size, and/or crystal phase, have been intensively studied and reviewed out of scientific interest and because of their technological importance.[1−4] In this respect, colloidal copper sulfide nanocrystals have not been studied as extensively as the lead and cadmium analogues. Copper sulfide is a p-type semiconductor due to copper vacancies, and colloidal nanocrystals have found application in solar cells,[5−7] cold cathodes,[8] nanoswitches,[9,10] and as building blocks for multinary phases such as $CuInS_2$. For technological applications that employ colloidal nanocrystals, control of crystal phase and size is of vital importance because the nanocrystal properties are intimately connected with these parameters. Hence, understanding the nanocrystal formation and growth, to ultimately gain size and phase control, is of large scientific and technological importance. The different synthesis strategies that have been used for colloidal copper sulfide nanocrystals are solventless thermolysis of copper thiolate precursors,[11−15] hydrothermal,[16,17] solvothermal,[18] liquid ammonia route,[19] thermal decomposition of different precursors in hot coordinating solvents,[20−30] and dispersion−decomposition.[31,32] The latter synthesis strategy has the advantage compared with the others that the synthesis can be performed in air and produce large quantities.

The morphology and size of $Cu_{2-x}S$ nanocrystals have been studied, and various morphologies (*i.e.*, spherical nanoparticles, nanodiscs, nanorods, or hexagonal nanoplates) can be synthesized by modifying the surface energy and/or surface reactivity. The control of the crystal phase is still difficult as copper sulfide easily forms different stoichiometric phases such as Cu_2S (γ- and β-chalcocite), $Cu_{1.98}S$ (djurleite), $Cu_{2-x}S$ (digenite), $Cu_{1.75}S$ (anilite), and CuS (covellite).[33−35] The copper content in digenite can vary from 1.8 to 2.[35] It has been shown that the particle size decreases with increasing dodecanethiol concentration; hence, the size is highly

* Address correspondence to bo@chem.au.dk.

Received for review November 5, 2013 and accepted April 9, 2014.

Published online April 09, 2014
10.1021/nn5010638

© 2014 American Chemical Society

interlinked with the thiol concentration in the reaction mixture.[23,26]

The synthesis strategies for copper sulfide are empirical as the reaction mechanisms are still not understood. *In situ* X-ray scattering has proven useful in uncovering the physical and chemical mechanisms controlling the characteristics of nanoparticles.[36−44] During the last 5 years, we have used various *in situ* X-ray scattering techniques to study hydrothermal reactions,[45−54] and here we employ the same technique for a nonaqueous solvent to study the formation, phase transition, and growth of nanocrystalline colloidal $Cu_{2-x}S$ in real time. The synthesis temperature was varied between 260 and 340 °C in steps of 20 °C in a pressurized (82.7 bar) sapphire capillary. To complement the *in situ* investigations, *ex situ* NMR and TEM data are also presented.

RESULTS

Phase Identification and Transition. The raw data from the experiment done at 280 °C, at selected times in the reaction, are shown in Figure 1. The *in situ* PXRD data reveal that there are several reactions and phase transitions occurring over time. The precursor is crystalline with almost equidistant peaks at low 2θ values (time −20 s). This can be interpreted as 3D stacked layers of Cu and S atoms with a large interlayer lattice dimension, where each layer of copper atoms are separated from one another by twice the length of the alkyl chain. All reflections are indexed as (0*k*0), with the (040) and (050) peaks indicated in Figure 1. The interlayer distance is 35.09 Å, in agreement with the expected formula $[CuSC_{12}H_{25}]$ and literature values.[14,55,56] The precursor also displays a broad amorphous peak underneath the crystalline part (10−15°).

After 180 and 1500 s, the phases β-chalcocite ($P6_3/mmc$) and high digenite ($Fm\bar{3}m$), respectively, are the only crystalline phases present when compared to the standard powder X-ray diffraction patterns. In Figure 1, the time evolution of the nanocrystals synthesized at 280 °C is shown, and on pp S2−S6 in Supporting Information, data are given for the other temperatures. When heat is applied, the crystalline precursor disappears and a completely amorphous phase appears. The broad amorphous peak observed in the precursor is shifted to lower scattering angles, which means that the amorphous material grows in correlation length and accordingly presumably plays an important role in the condensation. Sandhyarani *et al.* have found that the precursor undergoes three phase transitions during heating (crystalline I → crystalline II → mesophase → isotropic liquid), with the transition temperature to liquid happening at 151 °C.[56] These phase transitions were not observed in any of the present experiments because of the fast heating rate (the final temperatures of 260−340 °C are reached within 10 s, which is similar

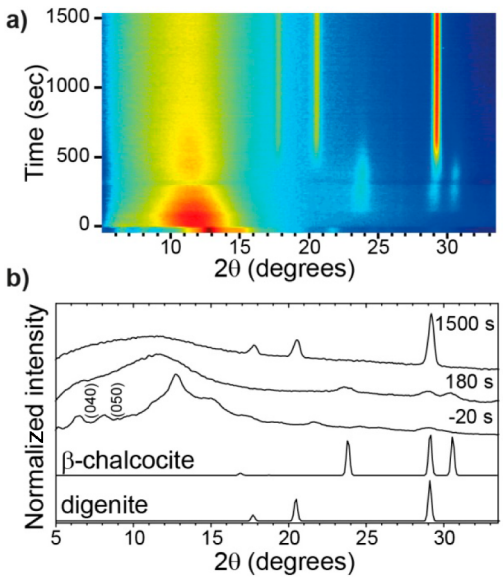

Figure 1. (a) Contour plot of raw powder X-ray diffraction data for the nanocrystals synthesized at 280 °C. (b) PXRD patterns at three different times and compared with standard patterns for the β-chalcocite ($P6_3/mmc$) and high digenite ($Fm\bar{3}m$) phase. Before the heat is applied, indicated by negative time, the $[CuSC_{12}H_{25}]$ crystalline precursor phase is present, and the (040) and (050) peaks are indexed.

to the detector time resolution of 9 s). A transition from amorphous phase to β-chalcocite (Cu_2S, $P6_3/mmc$) is observed in all experiments performed in the temperature interval of 260−320 °C. In addition in the experiments performed at temperatures from 280 to 320 °C, a transition from β-chalcocite to high digenite is observed. At 340 °C, high digenite is the only phase observed. Figure 2 shows the time evolution of the relative unit cell dimension, weight fraction, crystallite size, and normalized scale factor for $Cu_{2-x}S$ nanocrystals synthesized at 280 °C. In the first 400 s, the only phase present is β-chalcocite and then follows a transition period of 300 s, where both the β-chalcocite and high digenite phases are present, and in the end, only the high digenite phase is present. Data for the syntheses performed at 300 and 320 °C are shown in Supporting Information (pp S4 and S5). Both transitions are highly temperature-dependent. This is the first time that this phase transition is observed in the synthesis of $Cu_{2-x}S$ nanocrystals, although it is well-known that the transition takes place when a bulk sample of β-chalcocite is heated in air.[57] Nanocrystals have been synthesized *ex situ* in both an open flask experiment and a steel autoclave following a similar procedure. The open flask experiment (1 mmol, 220 °C, 1 h at ambient pressure)[32] results in 17 nm β-chalcocite nanocrystals that display a phase transition at 400 °C to high digenite; see Supporting Information (pp S7 and S8).[58] The ligands are completely removed at 330 °C with a 10.9% weight lost. The steel autoclave experiments were conducted at 260 and 340 °C (4 mL, 1.0 M precursor). This resulted in a mixture of β-chalcocite

nanocrystals and digenite nanocrystals at 260 °C, as shown in Supporting Information (p S9). Hence, the β-chalcocite to high digenite transition appears primarily driven by the synthesis temperature, though it cannot be excluded that the slight overpressure might help facilitate the formation of digenite. At 340 °C, phase-pure high digenite is formed and the estimated nanocrystal size is 29 nm; see Supporting Information (p S9).

Growth, Size, and Morphology. The nanocrystal growth is shown as a function of synthesis temperature in Figure 3. The growth rate of the β-chalcocite crystallites is slow at 260 °C, and the size stabilizes at around 7 nm (see pp S10−S14 in Supporting Information for details about crystallite size calculation). The growth rate increases with temperature. At 340 °C, the β-chalcocite growth period is believed to be faster than the time resolution; hence, a phase transition is not observable. The transition from β-chalcocite to high digenite does not appear to be a dissolution recrystallization process but rather a direct solid-state phase transition of the as-formed β-chalcocite nanocrystals to high digenite nanocrystals. This is based on the increase and decrease of the normalized scale factor occurring in parallel for the two phases, as well as the similar crystal growth rate and size for the two phases, as seen in Figures 2 and 3. The crystallite size of the high digenite phase is 10−11 nm, and it is not dependent on temperature after the transition has completed.

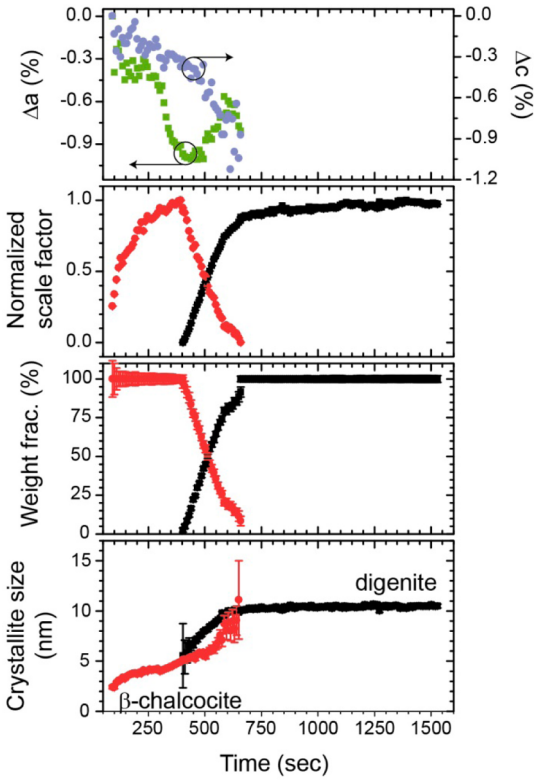

Figure 2. $Cu_{2-x}S$ nanocrystals synthesized at 280 °C. Relative unit cell axes changes of β-chalcocite ($\Delta a = (a(t) - a_0)/a_0$ and $\Delta c = (c(t) - c_0)/c_0$), with green markers for Δa and purple markers for Δc. Refined normalized scale factor, weight fractions, and crystallite size with red markers for β-chalcocite ($P6_3/mmc$) and black markers for high digenite ($Fm\bar{3}m$).

The unit cells of β-chalcocite and digenite are linked through the direction of close packed layers; that is, the tripled *c*-axis in β-chalcocite more or less corresponds to the doubled space diagonal of the digenite unit cell. The unit cell axes in β-chalcocite decrease as a function of time, as shown in Figure 4. Focusing on the data for the nanocrystals synthesized at 280 °C, it is evident that prior to the phase transition the *c*-axis decreases smoothly. After the phase transition, there is a change of slope and the *c*-axis decreases at a faster rate. The decrease in the *a*-axis exhibits a similar trend, but it is obscured by the overlap of peaks in the two phases, (110) in β-chalcocite and (220) in high digenite. Before the phase transition, the *a*-axis decreases with a gentle rate but then shows a steep decrease just prior to the phase transition. The *a*-axis increases after the transition is initiated, which originates from the overlap of peaks in the two phases, (110) in β-chalcocite and (220) in high digenite, as seen in Figure 1. These trends can be interpreted as follows. First, only the β-chalcocite phase is present, and the decrease in lattice parameter is due to the increasing nanocrystal size. The steeper slope in the two phase region is the cumulative effect of increasing nanocrystal size and the solid-to-solid phase transformation. The connection between size and relative change in unit cell is highly compound-dependent. As an example, this correlation has previously been investigated in our group for CeO_2 and

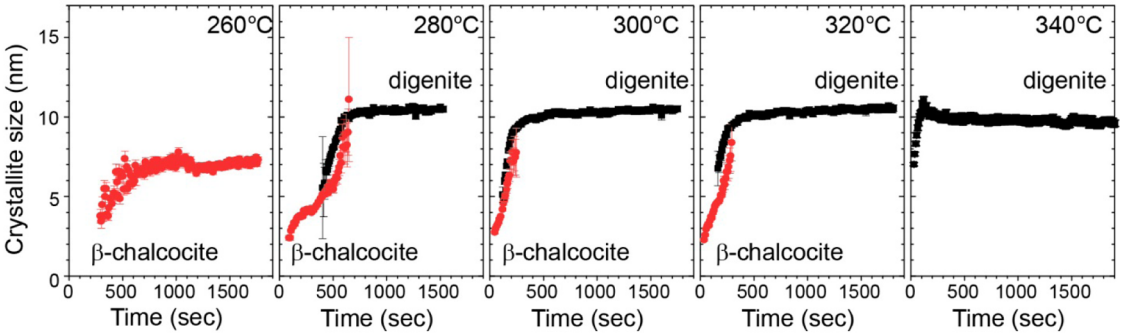

Figure 3. Crystallite size of copper sulfide nanocrystals for the different synthesis temperatures as a function of reaction time.

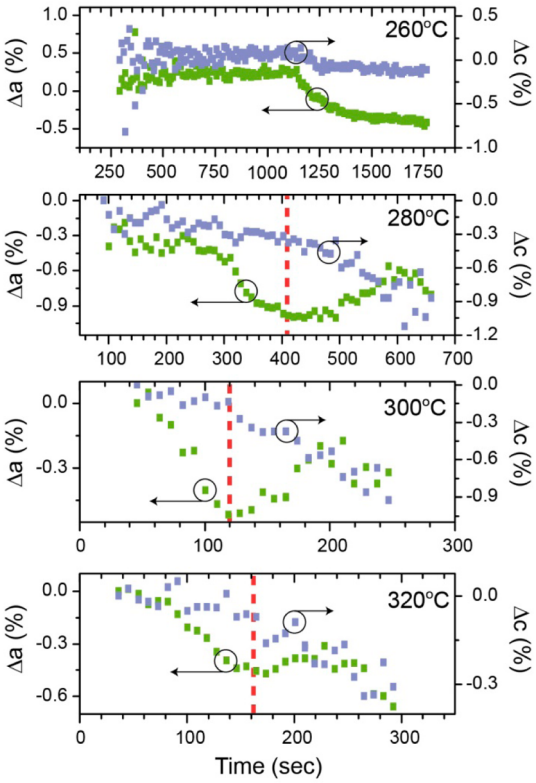

Figure 4. Relative unit cell changes of β-chalcocite ($\Delta a = (a(t) - a_0)/a_0$ and $\Delta c = (c(t) - c_0)/c_0$) for nanocrystals synthesized at 260, 280, 300, and 320 °C with green markers for Δa and purple markers for Δc. The red dotted line indicates the time where digenite nanocrystals first are observed in the PXRD patterns.

Fe_3O_4,[46,52] and for nanoparticles larger than 5 and 20 nm, no change is observed, respectively. Scanning electron microscopy energy-dispersive spectroscopic (SEM-EDX) data reveal that there are no significant differences in the copper content of the samples obtained at different temperatures, which might arise from averaging over a large area where some precursor might be present; see Supporting Information (p S15). Hence, the significant changes in unit cell axes presented here presumably originate from the structural transition, since the nanocrystal size is 5 nm when the transition initiates. A similar trend in unit cell axes is observed for the nanocrystals synthesized at 260 °C, albeit the axes do not decrease as much, indicating that the transition might have taken place if the reaction had been allowed to proceed for a longer period.

Size determination using PXRD data is based on the broadening of the Bragg peaks from the large assembly of nanocrystals studied in a diffraction experiment (see pp S10−S14 in Supporting Information). Transmission electron microscopy (TEM) gives a direct image of the particle size and morphology, including amorphous regions, but only a tiny fraction of the whole sample is studied and material characterization based solely on microscopy methods can thus be misleading. The size determined from TEM is the number-weighted average *particle size*, whereas PXRD analysis gives the volume-weighted *crystallite size*. In the present case, the samples studied by TEM and PXRD are not fully comparable since the thermal history and temperature profile in the two samples differ significantly. For the TEM sample, the synthesis is not stopped at the exact same time as the *in situ* synchrotron PXRD experiment. Furthermore, the entire content of the capillary is investigated in TEM. This includes reaction products from colder parts of the sapphire capillary, which are subject to a significant thermal gradient. The PXRD data refer to a narrow volume with a homogeneous temperature profile. Consequently, smaller nanocrystals as well as precursor material are observed in the TEM, as presented in the Supporting Information (p S16).

Representative TEM pictures of the as-synthesized nanocrystals are shown in Figure 5, and they show that

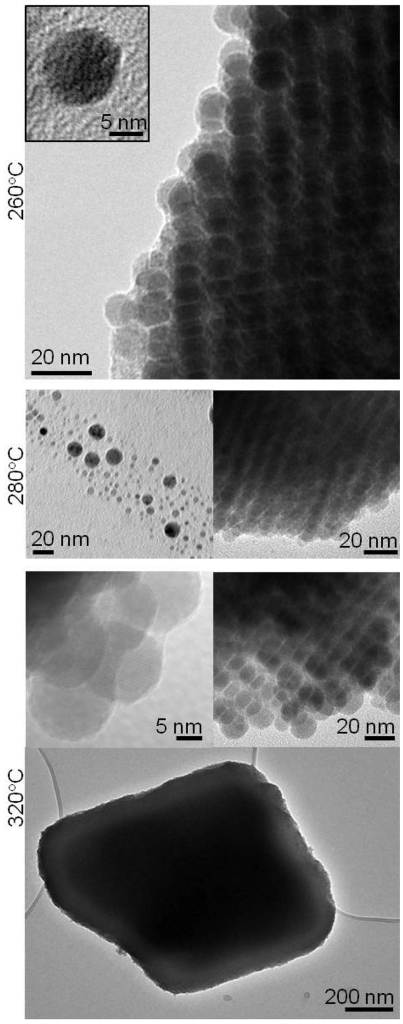

Figure 5. TEM pictures of $Cu_{2-x}S$ nanocrystals. Independent of synthesis temperature, the nanocrystals self-assemble into superlattices. The nanocrystals synthesized at 260 °C are slightly smaller than those synthesized at higher temperatures. The pictures for the nanocrystals synthesized at 280 °C show both the size distribution obtained due to the heating gradient and a part of a superlattice. At 320 °C, a large superlattice is shown with a zoom-in on parts of it.

the nanocrystals are spherical, single-crystalline domains, which self-assemble into close-packed superlattices independently of the synthesis temperature. In some cases, the superlattices are very large and extend up to a few micrometers in one dimension. In TEM, where the entire content of the capillary is investigated, a range of particle sizes are obtained in addition to the superlattices as shown for the nanocrystals synthesized at 280 °C. Both large and small nanocrystals are observed, which probably originates from the large temperature gradient along the capillary. The particle sizes determined from TEM are around 18 nm for the nanocrystals synthesized at 280 °C and above. Slightly smaller for the nanocrystals synthesized at 260 °C. This trend is in good agreement with results from the PXRD analysis, although the numerical values are larger (possibly due to an amorphous shell).

Formation. Copper has oxidation states of +2 and +1 in copper(II) acetate and the $Cu_{2-x}S$ nanocrystal, respectively; hence, the reaction must involve a reduction of copper.[59,60] The only functional molecule in the reaction mixture is dodecanethiol (DDT), which therefore must act both as a reducing agent and as a size and shape controller. The proton NMR spectra in Figure 6 show that DDT is oxidized to didodecyl disulfide at room temperature in the precursor. The chemical shifts (δ) for the α-methylene peaks in DDT and didodecyl disulfide are δ 2.53 ppm (quartet)[61] and δ 2.69 ppm (triplet),[62] respectively. The peaks in the proton NMR spectrum from the precursor molecules are diffuse, which can be ascribed to different effects, for example, viscous solution, paramagnetic impurities such as Cu^{2+} or that the precursor molecules are bound to the surface of copper sulfide containing nanoclusters.[63] Consequently, reaction schemes for the redox reaction in the precursor can be suggested:

$$2CH_3(CH_2)_{11}SH_{(DDT)} + 2Cu^{2+}_{(DDT)} \leftrightarrows 2H^{+}_{(DDT)} + 2Cu^{+}_{(DDT)} + CH_3(CH_2)_{11}S - S(CH_2)_{11}CH_{3(DDT)}$$

$$Cu^{+}_{(DDT)} + CH_3(CH_2)_{11}SH_{(DDT)} \leftrightarrows [CuSC_{12}H_{25}]_{(DDT)} + H^{+}_{(DDT)}$$

The PXRD in Figure 1 shows that a layered copper(I) thiolate structure as indicated by Espinet *et al.* as $[CuSC_{12}H_{25}]$[55,56] is present in the crystalline copper sulfide containing precursor. This is in agreement with the results from NMR. The proton NMR spectrum of the supernatant after the nanocrystal synthesis shows that all DDT has been oxidized during the reaction, despite the excess of DDT in the reaction and even though the whole content of the capillary, with a temperature gradient along the length, is investigated. The rate of the redox reaction taking place at room temperature must increase with temperature. The temperature in the colder parts of the capillary is fairly high (above 150 °C), and all the DDT is oxidized to didodecyl disulfide by first reducing copper and then through unidentified redox reactions occurring as the reaction proceeds.

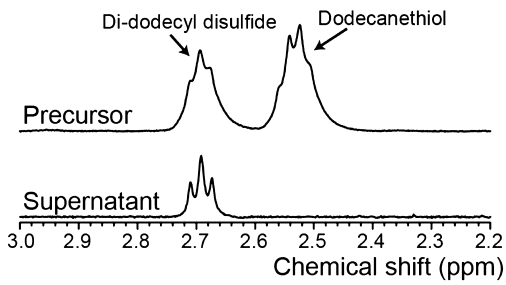

Figure 6. Proton NMR spectra showing the α-methylene chemical shifts in the precursor and supernatant for the nanocrystals synthesized at 320 °C. DDT (δ 2.53 ppm, q) and didodecyl disulfide (δ 2.69 ppm, t).

Transition Growth Kinetics and Activation Energy. The growth of high digenite crystallites from β-chalcocite, when only considering the solid-state nature, has been modeled with the Johnson–Mehl–Avrami model, where the reaction mechanism and activation energy can be extracted from the extent of reaction described by the equation $f = 1 - \exp[-k(t - t_0)^n]$.[64–66] Here, t is the time, t_0 is the first appearance of the high digenite phase, k is the rate constant, n is a number related to the mechanism, and f is the extent of the reaction. The extent of the reaction has been defined as $V(t)/V_{inf}$, where V_{inf} equals the final stable nanocrystal volume in the specific synthesis. Figure 7 shows $t - t_0$ as a function of the extent of the reaction, and the fits yield the following values: n(280 °C) = 1.03(3), n(300 °C) = 0.66(2), and n(320 °C) = 0.493(8). When n is between 0.54 and 0.62, is it an indication of a diffusion-controlled mechanism? 1.0–1.24 indicates a zero-order, first-order, or phase-boundary-controlled mechanism, and 2.0–3.0 indicates nucleation and growth control.[66,67] Values of n outside these specified ranges have no mechanistic meaning, and it is not possible on the basis of the value of n to distinguish between reaction mechanisms.[66] Hence, the individual rate laws have been tested and compared over the complete transition range. The phase transition displays second-order kinetics, which indicates that the growth is dependent not solely on the copper thiolate nanocluster concentration in the solute but also other factors, such as C–S cleavage. See pp S18–S20 in Supporting Information of details. Based on the fit to the Johnson–Mehl–Avrami equation, the activation energy, E_a, calculated by the Arrhenius equation $k(t) = A \exp(-E_a/(RT))$ can be obtained as the slope when T^{-1} is plotted as a function of ln(k). An activation energy of 47(7) kJ mol^{-1} is obtained.

DISCUSSION

The results show that under the present conditions the crystallite size of the high digenite phase does not change with time or temperature after the transition

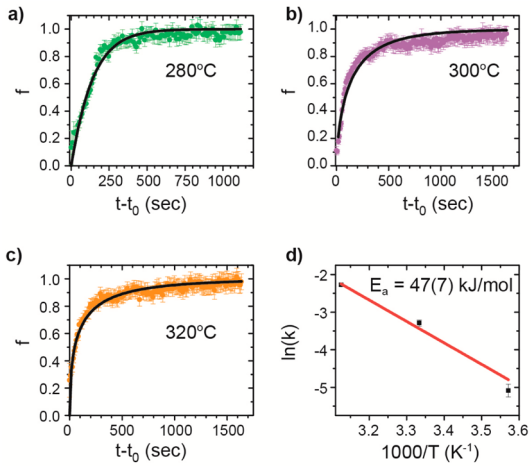

Figure 7. (a−c) Johnson−Mehl−Avrami plots for at the syntheses done at 280−320 °C. (d) Arrhenius plot with the obtained activation energy.

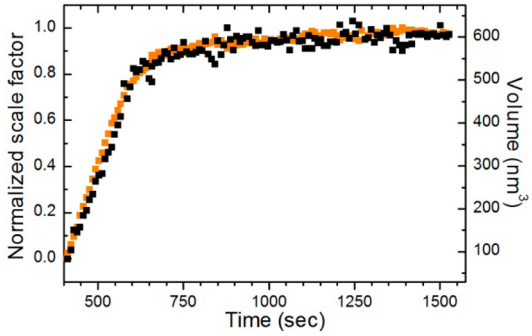

Figure 8. Normalized scale factor and nanocrystal volume of the high digenite phase plotted as a function of time for the synthesis at 280 °C.

from β-chalcocite has completed (the crystallite size settles at 11 nm). This is in contradiction with previous studies. Tang *et al.* found that the nanocrystal size increases with DDT content, temperature, and reaction time and with the morphology changing from spherical to hexagonal platelets with temperature.[27] Lim *et al.* found that the nanocrystal size of hexagonal platelets decreases with temperature and DDT content and that it increases with time.[23] It can be concluded that the nanocrystal size increases with reaction time. In accord with Du *et al.*, the nanocrystals display only one morphology (spherical) owing to the constant DDT/copper acetate ratio in the reactions performed in the present study.[25]

A possible explanation for the constant nanocrystal size based on the growth mechanism of the reaction is that all the copper thiolate nanoclusters in the illuminated area are used. This would lead to termination of the crystallite growth. Furthermore, the nanocrystal size increases to 29 nm when the precursor is heated in an autoclave, indicating that the crystalline growth is limited by diffusion in the capillary. The as-synthesized encapsulated larger particles do not react with each other, which is evident from Figure 8. Here it is seen that the curves of the Rietveld refinement scale factors and the nanoparticle volume can be superimposed. Hence, growth by Ostwald ripening does not occur, which indicates that the copper sulfide nanocrystals are assembled from $[CuSC_{12}H_{25}]$ building blocks, where the key step is the C−S bond cleavage. Judging from the initial formation of β-chalcocite, which is occurring at all temperatures except 340 °C (where the transformation likely occurs within the time resolution of our experiment), the $[CuSC_{12}H_{25}]$ building blocks lead to β-chalcocite nanocrystals, which are then converted to digenite nanocrystals through a solid-to-solid phase transition. The calculated activation energy for the formation of digenite (47 kJ/mol) cannot be interpreted as the activation energy of the solid-to-solid phase transition, because other contributions have to be taken into account. In the formation of copper sulfide nanocrystals, the limiting step is the C−S bond cleavage, so the calculated activation energy is rather the accumulated energy input for the C−S bond cleavage as well as the phase transition. The mechanism underlying the C−S bond cleavage is believed to be dependent on different parameters, *e.g.* substituting copper(II) acetate with copper(II) acetylacetonate have been shown by Han *et al.* to result in djurleite.[31] It is beyond the scope of this paper to investigate the C−S cleavage mechanism.

CONCLUSION

In situ synchrotron X-ray scattering data provide information about how to control the size and phase of colloidal copper sulfide as a function of time and temperature. Highly monodisperse β-chalcocite spherical nanocrystals were obtained when the synthesis temperature was 260 °C. Above this temperature, a direct solid-state phase transition of as-prepared β-chalcocite nanocrystals to high digenite takes place, which is also evident from the decrease in lattice constant of the β-chalcocite phase prior to the detection of the high digenite phase in the X-ray patterns. The crystallite size of highly monodisperse β-chalcocite formed at 260 °C extracted from X-ray analysis is 7 nm. The subsequent TEM analysis shows that the particle size is 16 nm. For the high digenite nanocrystals, the crystallite and particle sizes are 11 and 18 nm, respectively, regardless of the synthesis temperature. The monodispersity and morphology are not changed upon phase transition. Proton NMR on the supernatant and precursor reveal that the redox reaction takes place in the precursor, where DDT is oxidized to didodecyl disulfide. All DDT has been oxidized when the reaction is complete, because the temperature in the capillary accelerates the redox reaction.

Johnson−Mehl−Avrami analysis of the *in situ* data show that the growth of high digenite follows a complex reaction pathway. An activation energy of

47(7) kJ mol^{-1} is obtained for the transition of β-chalcocite to high digenite nanocrystals, which has to be interpreted as a sum of different contributions, such as C−S bond cleavage, growth, and phase transition. It is shown that the transition rate of β-chalcocite to high digenite increases with temperature, and monodisperse high digenite 11 nm sized nanocrystals can be obtained after 200 s at 340 °C.

METHODS

Precursor Synthesis and *In Situ* Experiment. All the reagents were used as purchased without further purification. Pale yellow viscous suspensions of [$CuSC_{12}H_{25}$] in 1-dodecanethiol (purity ≥98%) were made by adding 1.9943 g $(CH_3COO)_2Cu\cdot H_2O$ (purity >98%) in 10 mL of 1-dodecanethiol (1.00 M solution).

The *in situ* experiments were performed at beamline I711, MAX II[68] (MAX-lab, Lund, Sweden). The setup used for the experiments has been described in detail by Becker *et al.*[69] The viscous precursor solution was injected into a thin sapphire capillary (inner diameter 0.7 mm), pressurized with water to 82.7 bar. The reaction was initiated by blowing a stream of hot air onto the sapphire capillary. Due to the efficiency of the heater and the small volume of the capillary, the desired temperature was reached within 10 s. The temperatures for the different Cu_2S syntheses were 260−340 °C in steps of 20 °C. X-ray patterns were collected before the heating was applied. The wavelength was calibrated by a NIST LaB_6 standard, and the refined values found to vary in a narrow range between 0.9995 and 1.0018 Å. The time resolution was 9 s. Each experiment was allowed to run for at least 25 min at constant temperature and pressure. The X-rays were detected by an Oxford Diffraction Titan CCD detector with a detector-to-sample distance of approximately 90 mm (calibrated from NIST LaB_6 standard).

^{1}H NMR, TEM, and SEM-EDX. The product in the sapphire capillary was collected after the reaction had terminated by replacing the product with ethanol. Due to the temperature profile over the length of the capillary, with a hot spot in the region of X-ray illumination (see p S21 in Supporting Information), a sample with a mixture of different reaction temperatures was collected. The product was washed with ethanol and centrifuged in order to separate supernatant and the nanocrystals. The supernatant was dried with $MgSO_4$, filtered, and concentrated on a rotary evaporator in order to remove excess ethanol and water. The boiling point of dodecanethiol, didodecyl disulfide, and dodecane is above 200 °C.

TEM pictures were acquired with a Phillips CM20 microscope with an acceleration voltage of 200 keV. SEM was performed using a Nova NanoSEM 600 (FEI Co., The Netherlands). Energy-dispersive X-ray spectroscopic (EDX) was performed using EDAX Genesis detector attached to the SEM column. The samples were prepared by placing a droplet of the nanocrystals suspended in ethanol on a carbon-coated copper grid and carbon film for TEM and SEM, respectively. Liquid phase proton NMR was acquired on a Varian AS 400 spectrometer, running at 400 MHz for ^{1}H. Samples were made by dissolving either the concentrate supernatant or the precursor gel in $CDCl_3$. Chemical shifts (δ) are reported in parts per million relative to residual solvent signals from $CDCl_3$ (7.26 ppm for ^{1}H NMR).

Data Integration and Analysis. The 2D diffraction frames were integrated to 1D patterns in Fit2D,[70] subsequent to masking of single-crystal diffraction peaks originating from the sapphire capillary. The integrated PXRD data were analyzed by sequential Rietveld refinement in the FullProf Suite program package.[71] Details on the refinements can be found in Supporting Information. The weight fractions of the crystalline phases as well as the volume-weighted size of the crystalline nanocrystals were extracted from the refined parameters corrected for instrumental broadening. Spherical harmonics were used to simulate the average morphology and size of the nanocrystals.[72] It was assumed that the particles are spherical, in agreement with TEM pictures; see pp S10−S14 in Supporting Information for additional particle shape analysis and discussion.

Conflict of Interest: The authors declare no competing financial interest.

Acknowledgment. The work was supported by the Danish National Research Foundation (Center for Materials Crystallography, DNRF93) and the Danish Research Council for Nature and Universe (Danscatt). MAX-lab and Spring8 (RIKEN) are acknowledged for beam time. Per S. Christensen, Henrik L. Andersen, Espen D. Bøjesen, Dr. Kirsten M. Ø. Jensen, Dr. Mogens Christensen, and Dr. Nina Lock are thanked for assistance during the experiments at MAX-lab. Tore K. Johansen is thanked for assistance with proton NMR measurements.

Supporting Information Available: Detailed description of the sequential Rietveld refinement, calculation of nanocrystal size from spherical harmonics, Rietveld refinement example, contour plot of raw data, weight fractions for 300 and 320 °C, SEM-EDX data, TEM picture with three different phases, reaction-order modeling of the kinetics for the transition from β-chalcocite to high digenite and NMR spectra, information on *ex situ* synthesized nanocrystals including heating ramp synchrotron PXRD patterns, multitemperature synchrotron PXRD patterns, TEM pictures, thermogravimetric data, and Rietveld refinement. This material is available free of charge *via* the Internet at http://pubs.acs.org.

REFERENCES AND NOTES

1. Alivisatos, A. P. Semiconductor Clusters, Nanocrystals, and Quantum Dots. *Science* **1996**, *271*, 933–937.
2. Murray, C. B.; Kagan, C. R.; Bawendi, M. G. Synthesis and Characterization of Monodisperse Nanocrystals and Close-Packed Nanocrystal Assemblies. *Annu. Rev. Mater. Sci.* **2000**, *30*, 545–610.
3. Burda, C.; Chen, X.; Narayanan, R.; El-Sayed, M. A. Chemistry and Properties of Nanocrystals of Different Shapes. *Chem. Rev.* **2005**, *105*, 1025–1102.
4. Talapin, D. V.; Lee, J.-S.; Kovalenko, M. V.; Shevchenko, E. V. Prospects of Colloidal Nanocrystals for Electronic and Optoelectronic Applications. *Chem. Rev.* **2010**, *110*, 389–458.
5. Lee, H.; Yoon, S. W.; Kim, E. J.; Park, J. *In-Situ* Growth of Copper Sulfide Nanocrystals on Multiwalled Carbon Nanotubes and Their Application as Novel Solar Cell and Amperometric Glucose Sensor Materials. *Nano Lett.* **2007**, *7*, 778–784.
6. Wu, Y.; Wadia, C.; Ma, W.; Sadtler, B.; Alivisatos, A. P. Synthesis and Photovoltaic Application of Copper(I) Sulfide Nanocrystals. *Nano Lett.* **2008**, *8*, 2551–2555.
7. Lin, M.-C.; Lee, M.-W. $Cu_{2-x}S$ Quantum Dot-Sensitized Solar Cells. *Electrochem. Commun.* **2011**, *13*, 1376–1378.
8. Chen, J.; Deng, S. Z.; Xu, N. S.; Wang, S.; Wen, X.; Yang, S.; Yang, C.; Wang, J.; Ge, W. Field Emission from Crystalline Copper Sulphide Nanowire Arrays. *Appl. Phys. Lett.* **2002**, *80*, 3620–3622.
9. Sakamoto, T.; Sunamura, H.; Kawaura, H.; Hasegawa, T.; Nakayama, T.; Aono, M. Nanometer-Scale Switches Using Copper Sulfide. *Appl. Phys. Lett.* **2003**, *82*, 3032–3034.
10. Chen, L.; Xia, Y.; Liang, X.; Yin, K.; Yin, J.; Liu, Z.; Chen, Y. Nonvolatile Memory Devices with Cu_2S and Cu-Pc Bilayered Films. *Appl. Phys. Lett.* **2007**, *91*, 073511.
11. Larsen, T. H.; Sigman, M. B.; Ghezelbash, A.; Doty, R. C.; Korgel, B. A. Solventless Synthesis of Copper Sulfide Nanorods by Thermolysis of a Single Source Thiolate-Derived Precursor. *J. Am. Chem. Soc.* **2003**, *125*, 5638–5639.
12. Sigman, M. B.; Ghezelbash, A.; Hanrath, T.; Saunders, A. E.; Lee, F.; Korgel, B. A. Solventless Synthesis of Monodisperse Cu_2S Nanorods, Nanodisks, and Nanoplatelets. *J. Am. Chem. Soc.* **2003**, *125*, 16050–16057.

13. Tian, C.; Kang, Z.; Wang, E.; Gao, L.; Wang, C.; Xu, L.; Hu, C. Synthesis of Dodecanethiolate-Protected Cu_2S Nanoparticles in a Two-Phase System. *Mater. Lett.* **2005**, *59*, 1156–1160.
14. Chen, Y.-B.; Chen, L.; Wu, L.-M. The Structure-Controlling Solventless Synthesis and Optical Properties of Uniform Cu_2S Nanodisks. *Chem.—Eur. J.* **2008**, *14*, 11069–11075.
15. Mott, D.; Yin, J.; Engelhard, M.; Loukrakpam, R.; Chang, P.; Miller, G.; Bae, I.-T.; Chandra Das, N.; Wang, C.; Luo, J.; *et al.* From Ultrafine Thiolate-Capped Copper Nanoclusters toward Copper Sulfide Nanodiscs: A Thermally Activated Evolution Route. *Chem. Mater.* **2010**, *22*, 261–271.
16. Lu, Q.; Gao, F.; Zhao, D. One-Step Synthesis and Assembly of Copper Sulfide Nanoparticles to Nanowires, Nanotubes, and Nanovesicles by a Simple Organic Amine-Assisted Hydrothermal Process. *Nano Lett.* **2002**, *2*, 725–728.
17. Zhuang, Z.; Peng, Q.; Zhang, B.; Li, Y. Controllable Synthesis of Cu_2S Nanocrystals and Their Assembly into a Superlattice. *J. Am. Chem. Soc.* **2008**, *130*, 10482–10483.
18. An, C.; Wang, S.; He, J.; Wang, Z. A Composite-Surfactants-Assisted-Solvothermal Process to Copper Sulfide Nanocrystals. *J. Cryst. Growth* **2008**, *310*, 266–269.
19. Henshaw, G.; Parkin, I. P.; Shaw, G. A. Convenient, Room-Temperature Liquid Ammonia Routes to Metal Chalcogenides. *J. Chem. Soc., Dalton Trans.* **1997**, 231–236.
20. Kuzuya, T.; Yamamuro, S.; Hihara, T.; Sumiyama, K. Water-Free Solution Synthesis of Monodisperse Cu_2S Nanocrystals. *Chem. Lett.* **2004**, *33*, 352–353.
21. Ghezelbash, A.; Korgel, B. A. Nickel Sulfide and Copper Sulfide Nanocrystal Synthesis and Polymorphism. *Langmuir* **2005**, *21*, 9451–9456.
22. Itoh, K.; Kuzuya, T.; Sumiyama, K. Morphology and Composition-Controls of Cu_xS Nanocrystals Using Alkyl-Amine Ligands. *Mater. Trans.* **2006**, *47*, 1953–1956.
23. Lim, W. P.; Wong, C. T.; Ang, S. L.; Low, H. Y.; Chin, W. S. Phase-Selective Synthesis of Copper Sulfide Nanocrystals. *Chem. Mater.* **2006**, *18*, 6170–6177.
24. Kuzuya, T.; Itoh, K.; Ichidate, M.; Wakamatsu, T.; Fukunaka, Y.; Sumiyama, K. Facile Synthesis of Nearly Monodispersed Copper Sulfide Nanocrystals. *Electrochim. Acta* **2007**, *53*, 213–217.
25. Du, X.-S.; Mo, M.; Zheng, R.; Lim, S.-H.; Meng, Y.; Mai, Y.-W. Shape-Controlled Synthesis and Assembly of Copper Sulfide Nanoparticles. *Cryst. Growth Des.* **2008**, *8*, 2032–2035.
26. Li, S.; Wang, H.; Xu, W.; Si, H.; Tao, X.; Lou, S.; Du, Z.; Li, L. S. Synthesis and Assembly of Monodisperse Spherical Cu_2S Nanocrystals. *J. Colloid Interface Sci.* **2009**, *330*, 483–487.
27. Tang, A.; Qu, S.; Li, K.; Hou, Y.; Teng, F.; Cao, J.; Wang, Y.; Wang, Z. One-Pot Synthesis and Self-Assembly of Colloidal Copper(I) Sulfide Nanocrystals. *Nanotechnology* **2010**, *21*, 285602.
28. Kanehara, M.; Arakawa, H.; Honda, T.; Saruyama, M.; Teranishi, T. Large-Scale Synthesis of High-Quality Metal Sulfide Semiconductor Quantum Dots with Tunable Surface-Plasmon Resonance Frequencies. *Chem.—Eur. J.* **2012**, *18*, 9230–9238.
29. Kruszynska, M.; Borchert, H.; Bachmatiuk, A.; Rümmeli, M. H.; Büchner, B.; Parisi, J.; Kolny-Olesiak, J. Size and Shape Control of Colloidal Copper(I) Sulfide Nanorods. *ACS Nano* **2012**, *6*, 5889–5896.
30. Zhang, Y.; Li, X.; Xu, W.; Li, S.; Wang, H.; Li, L. S. The Size Controlled Synthesis and Self-Assembled of Monodisperse Cu_2S Nanocrystals. *Mater. Lett.* **2012**, *67*, 117–120.
31. Han, W.; Yi, L.; Zhao, N.; Tang, A.; Gao, M.; Tang, Z. Synthesis and Shape-Tailoring of Copper Sulfide/Indium Sulfide-Based Nanocrystals. *J. Am. Chem. Soc.* **2008**, *130*, 13152–13161.
32. Zhuang, Z.; Lu, X.; Peng, Q.; Li, Y. A Facile "Dispersion-Decomposition" Route to Metal Sulfide Nanocrystals. *Chem.—Eur. J.* **2011**, *17*, 10445–10452.
33. Koch, D. F. A.; McIntyre, R. J. The Application of Reflectance Spectroscopy to a Study of the Anodic Oxidation of Cuprous Sulphide. *J. Electroanal. Chem.* **1976**, *71*, 285–296.
34. Vaughan, D. J.; Craig, J. R. *Mineral Chemistry of Metal Sulfides*; Harland, W. B.; Agrell, S. O.; Cook, A. H.; Hughnes, N. F., Eds.; Cambridge University Press: Cambridge, UK, 1978; pp 290−292.
35. Lee, B.-J.; Sundman, B.; Kim, S. I.; Chin, K.-G. Thermodynamic Calculations on the Stability of Cu_2S in Low Carbon Steels. *ISIJ. Int.* **2007**, *47*, 163–171.
36. Clausen, B. S.; Steffensen, G.; Fabius, B.; Villadsen, J.; Feidenhans'l, R.; Topsøe, H. *In Situ* Cell for Combined XRD and On-Line Catalysis Tests: Studies of Cu-Based Water Gas Shift and Methanol Catalysts. *J. Catal.* **1991**, *132*, 524–535.
37. Michailovski, A.; Grunwaldt, J.-D.; Baiker, A.; Kiebach, R.; Bensch, W.; Patzke, G. R. Studying the Solvothermal Formation of MoO_3 Fibers by Complementary *In Situ* EXAFS/EDXRD Techniques. *Angew. Chem., Int. Ed.* **2005**, *44*, 5643–5647.
38. Norby, P. *In-Situ* XRD as a Tool To Understanding Zeolite Crystallization. *Curr. Opin. Colloid Interface Sci.* **2006**, *11*, 118–125.
39. Clearfield, A.; Tripathi, A.; Medvedev, D.; Celestian, A. J.; Parise, J. B. *In Situ* Type Study of Hydrothermally Prepared Titanates and Silicotitanates. *J. Mater. Sci.* **2006**, *41*, 1325–1333.
40. Shen, X.-F.; Ding, Y.-S.; Hanson, J. C.; Aindow, M.; Suib, S. L. *In Situ* Synthesis of Mixed-Valent Manganese Oxide Nanocrystals: An *In Situ* Synchrotron X-ray Diffraction Study. *J. Am. Chem. Soc.* **2006**, *128*, 4570–4571.
41. Mitchell, S.; Biswick, T.; Jones, W.; Williams, G.; O'Hare, D. A Synchrotron Radiation Study of the Hydrothermal Synthesis of Layered Double Hydroxides from MgO and Al_2O_3 Slurries. *Green Chem.* **2007**, *9*, 373–378.
42. Du, Y.; Ok, K. M.; O'Hare, D. A Kinetic Study of the Phase Conversion of Layered Cobalt Hydroxides. *J. Mater. Chem.* **2008**, *18*, 4450–4459.
43. Cheong, S.; Watt, J.; Ingham, B.; Toney, M. F.; Tilley, R. D. *In Situ* and *Ex Situ* Studies of Platinum Nanocrystals: Growth and Evolution in Solution. *J. Am. Chem. Soc.* **2009**, *131*, 14590–14595.
44. Pienack, N.; Bensch, W. *In-Situ* Monitoring of the Formation of Crystalline Solids. *Angew. Chem., Int. Ed.* **2011**, *50*, 2014–2034.
45. Jensen, H.; Bremholm, M.; Nielsen, R. P.; Joensen, K. D.; Pedersen, J. S.; Birkedal, H.; Chen, Y.-S.; Almer, J.; Søgaard, E. G.; Iversen, S. B.; *et al.* *In Situ* High-Energy Synchrotron Radiation Study of Sol−Gel Nanoparticle Formation in Supercritical Fluids. *Angew. Chem., Int. Ed.* **2007**, *46*, 1113–1116.
46. Bremholm, M.; Felicissimo, M.; Iversen, B. B. Time-Resolved *In Situ* Synchrotron X-ray Study and Large-Scale Production of Magnetite Nanoparticles in Supercritical Water. *Angew. Chem., Int. Ed.* **2009**, *48*, 4788–4791.
47. Bremholm, M.; Becker-Christensen, J.; Iversen, B. B. High-Pressure, High-Temperature Formation of Phase-Pure Monoclinic Zirconia Nanocrystals Studied by Time-Resolved *In Situ* Synchrotron X-ray Diffraction. *Adv. Mater.* **2009**, *21*, 3572–3575.
48. Lock, N.; Bremholm, M.; Christensen, M.; Almer, J.; Chen, Y.-S.; Iversen, B. B. *In Situ* High-Energy Synchrotron Radiation Study of Boehmite Formation, Growth, and Phase Transformation to Alumina in Sub- and Supercritical Water. *Chem.—Eur. J.* **2009**, *15*, 13381–13390.
49. Tyrsted, C.; Becker, J.; Hald, P.; Bremholm, M.; Pedersen, J. S.; Chevallier, J.; Cerenius, Y.; Iversen, S. B.; Iversen, B. B. *In-Situ* Synchrotron Radiation Study of Formation and Growth of Crystalline $Ce_xZr_{1-x}O_2$ Nanoparticles Synthesized in Supercritical Water. *Chem. Mater.* **2010**, *22*, 1814–1820.
50. Lock, N.; Christensen, M.; Jensen, K. M. Ø.; Iversen, B. B. Rapid One-Step Low-Temperature Synthesis of Nanocrystalline γ-Al_2O_3. *Angew. Chem., Int. Ed.* **2011**, *50*, 7045–7047.
51. Jensen, K. M. Ø.; Christensen, M.; Juhás, P.; Tyrsted, C.; Bøjesen, E. D.; Lock, N.; Billinge, S. J. L.; Iversen, B. B. Revealing the Mechanisms behind SnO_2 Nanoparticle Formation and Growth during Hydrothermal Synthesis: An *In Situ* Total Scattering Study. *J. Am. Chem. Soc.* **2012**, *134*, 6785–6792.
52. Tyrsted, C.; Jensen, K. M. Ø.; Bøjesen, E. D.; Lock, N.; Christensen, M.; Billinge, S. J. L.; Iversen, B. B. Understanding the Formation and Evolution of Ceria Nanoparticles under Hydrothermal Conditions. *Angew. Chem., Int. Ed.* **2012**, *51*, 9030–9033.

53. Eltzholtz, J. R.; Tyrsted, C.; Jensen, K. M. Ø.; Bremholm, M.; Christensen, M.; Becker-Christensen, J.; Iversen, B. B. Pulsed Supercritical Synthesis of Anatase TiO_2 Nanoparticles in a Water−Isopropanol Mixture Studied by *In Situ* Powder X-ray Diffraction. *Nanoscale* **2013**, *5*, 2372–2378.
54. Nørby, P.; Jensen, K. M. Ø.; Lock, N.; Christensen, M.; Iversen, B. B. *In Situ* Synchrotron Powder X-ray Diffraction Study of Formation and Growth of Yttrium and Ytterbium Aluminum Garnet Nanoparticles in Sub- and Supercritical Water. *RSC Adv.* **2013**, *3*, 15368–15374.
55. Espinet, P.; Lequerica, M. C.; Martín-Alvarez, J. M. Synthesis, Structural Characterization and Mesogenic Behavior of Copper(I) *n*-Alkylthiolates. *Chem.—Eur. J.* **1999**, *5*, 1982–1986.
56. Sandhyarani, N.; Pradeep, T. An Investigation of the Structure and Properties of Layered Copper Thiolates. *J. Mater. Chem.* **2001**, *11*, 1294–1299.
57. Buerger, N. W. X-ray Evidence of the Existence of the Mineral Digenite, Cu_9S_5. *Am. Mineral.* **1942**, *27*, 712–716.
58. Rivest, J. B.; Fong, L.-K.; Jain, P. K.; Toney, M. F.; Alivisatos, A. P. Size Dependence of a Temperature-Induced Solid−Solid Phase Transition in Copper(I) Sulfide. *J. Phys. Chem. Lett.* **2011**, *2*, 2402–2406.
59. Brust, M.; Blass, P. M.; Bard, A. J. Self-Assembly of Photoluminescent Copper(I)−Dithiol Multilayer Thin Films and Bulk Materials. *Langmuir* **1997**, *13*, 5602–5607.
60. Johnson, S.; Bronowska, A.; Chan, J.; Evans, D.; Davies, A. G.; Wälti, C. Redox-Induced Conformational Change in Mercaptoalkanoic Acid Multilayer Films. *Langmuir* **2012**, *28*, 6632–6637.
61. Conte, P.; Carotenuto, G.; Piccolo, A.; Perlo, P.; Nicolais, L. NMR-Investigation of the Mechanism of Silver Mercaptide Thermolysis in Amorphous Polystyrene. *J. Mater. Chem.* **2007**, *17*, 201–205.
62. Wang, L.; Clive, D. L. J. [[(*tert*-Butyl)dimethylsilyl]oxy]-methyl Group for Sulfur Protection. *Org. Lett.* **2011**, *13*, 1734–1737.
63. Hasan, M.; Bethell, D.; Brust, M. The Fate of Sulfur-Bound Hydrogen on Formation of Self-Assembled Thiol Monolayers on Gold: ^{1}H NMR Spectroscopic Evidence from Solutions of Gold Clusters. *J. Am. Chem. Soc.* **2002**, *124*, 1132–1133.
64. Avrami, M. Kinetics of Phase Change. I General Theory. *J. Chem. Phys.* **1939**, *7*, 1103–1112.
65. Johnson, W. A.; Mehl, R. F. Reaction Kinetics in Processes of Nucleation and Growth. *Trans. Am. Inst. Min., Metall. Pet. Eng.* **1939**, *135*, 416–442.
66. Rossetti, G. A.; Watson, D. J.; Newnham, R. E.; Adair, J. H. Kinetics of the Hydrothermal Crystallization of the Perovskite Lead Titanate. *J. Cryst. Growth* **1992**, *116*, 251–259.
67. Hancock, J. D.; Sharp, J. H. Method of Comparing Solid-State Kinetic Data and Its Application to the Decomposition of Kaolinite, Brucite, and $BaCO_3$. *J. Am. Ceram. Soc.* **1972**, *55*, 74–77.
68. Cerenius, Y.; Ståhl, K.; Svensson, L. A.; Ursby, T.; Oskarsson, A.; Albertsson, J.; Liljas, A. The Crystallography Beamline I711 at MAX II. *J. Synchrotron Radiat.* **2000**, *7*, 203–208.
69. Becker, J.; Bremholm, M.; Tyrsted, C.; Pauw, B.; Jensen, K. M. Ø.; Eltzholtz, J.; Christensen, M.; Iversen, B. B. Experimental Setup for *In Situ* X-ray SAXS/WAXS/PDF Studies of the Formation and Growth of Nanoparticles in Near- and Supercritical Fluids. *J. Appl. Crystallogr.* **2010**, *43*, 729–736.
70. Hammersley, A. P.; Svensson, S. O.; Hanfland, M.; Fitch, A. N.; Häusermann, D. Two-Dimensional Detector Software: From Real Detector to Idealised Image or Two-Theta Scan. *High Press. Res.* **1996**, *14*, 235–248.
71. Rodríguez-Carvajal, J. Recent Advances in Magnetic Structure Determination by Neutron Powder Diffraction. *Physica B* **1993**, *192*, 55–69.
72. Järvinen, M. Application of Symmetrized Harmonics Expansion to Correction of the Preferred Orientation Effect. *J. Appl. Crystallogr.* **1993**, *26*, 525–531.